Field surveys of September 2018 landslide-generated waves in the Apporo dam reservoir, Japan: Combined hazard from the concurrent occurrences of a typhoon and an earthquake

Mohammad Heidarzadeh[*1], Hiroko Miyazaki[2], Takeo Ishibe[3], Hiroshi Takagi[4], Ramtin Sabeti[2]

[1] Department of Architecture and Civil Engineering, University of Bath, Bath BA2 7AY, UK
[2] Department of Civil & Environmental Engineering, Brunel University London, Uxbridge UB8 3PH, UK
[3] Association for the Development of Earthquake Prediction, Tokyo, 101-0064, Japan
[4] School of Environment and Society, Tokyo Institute of Technology, Tokyo, 152-8550, Japan

Published in: **"Landslides"**
https://doi.org/10.1007/s10346-022-01959-8

*** Correspondence to:**

Mohammad Heidarzadeh, PhD
Associate Professor
Department of Architecture and Civil Engineering,
University of Bath, Bath BA2 7AY,
United Kingdom.
Email: mhk58@bath.ac.uk
Website: https://researchportal.bath.ac.uk/en/persons/mohammad-heidarzadeh-kolaei
ORCID: https://orcid.org/0000-0002-1112-1276

Abstract

We report and analyze a case study of landslide-generated waves that occurred in the Apporo dam reservoir (Hokkaido, Japan) culminating from the rare incident of hazard combination from the September 2018 Typhoon Jebi and Hokkaido earthquake (M_w 6.6 on 5 September 2018). The typhoon and earthquake were concurrent and produced thousands of landslides in the area by the combined effects of soil saturation and ground acceleration. Here, we report the results of our field surveys of the landslides that occurred around the Apporo dam and generated damaging waves in the reservoir. We identified six landslides at a close distance to the dam body; the largest one has a length of 330 m, a maximum width of 140 m and a volume of 71,400 m^3. We measured wave runup at a single point with height of 5.3 m for the landslide-generated wave in the reservoir and recorded the damage made to the revetments at the reservoir banks. By considering the locations of the landslides and their potential propagation paths, we speculate that possibly three of the six surveyed landslides contributed to the measured wave runup. The surveyed runup was reproduced by inputting landslide parameters into two independent empirical equations; however, other independent empirical relationships failed to reproduce the observed runup. Our field data from the Apporo dam can be used to improve the quality of predictions made by empirical equations and to encourage further research on this topic. In addition, our field data serves as a call for strengthening dams' safety to landslide-generated waves in reservoirs.

Keywords: Earthquake; Typhoon; Landslide; Landslide Impulse Wave; Hydraulics; Dam Engineering; Hazard Combinations.

1. Introduction

The Atsuma area of Hokkaido (Japan) was the site of thousands of destructive landslides on 5 September 2018 (UTC) triggered by an M_w 6.6 earthquake. According to the United States Geological Survey (USGS), this reverse-faulting earthquake occurred at 42.686°N 141.929°E with an origin time of 18:07:59 (UTC) and a focal depth of 35.0 km (Figure 1a). Nearly six thousand landslides were reported in the area, taking the lives of 36 people (Yamagishi and Yamazaki 2018; Zhang et al. 2019; Aimaiti et al. 2019). The earthquake was approximately concurrent with the passage of Typhoon Jebi over Hokkaido, which brought torrential rainfall in the area and saturated soils on mountain slopes before the earthquake occurrence (Le et al. 2019; Aimaiti et al. 2019). Typhoon Jebi, which was active over Japan in the period 3-6 September 2018, was the strongest typhoon to hit Japan since 1993 and caused severe destruction and 13 deaths (Le et al. 2019; Heidarzadeh and Rabinovich, 2021).

Following the September 2018 Hokkaido earthquake, landslide-generated waves were generated in the Apporo dam reservoir, which produced some damage to reservoir banks. The hazard from landslide-generated waves in dam reservoirs has been long known (e.g., Schnitter 1964; Schuster and Wieczorek 2002; Ataie-Ashtiani and Yavari-Ramshe 2011; Ersoy et al. 2019; Evers et al. 2019a, 2019b; Evers and Boes, 2019). One of the most destructive landslide-generated waves worldwide

66 occurred in the Vajont dam reservoir (Italy) in October 1963 killing more than 2,000 people (Bosa and
67 Petti 2011; Vacondio et al. 2013; Roberts et al., 2014). Miyagi et al. (2011) reported a large landslide
68 (volume of more than 67 million m^3) that occurred in the Aratozawa Dam area (Tohoku, Japan) in
69 June 2008 following an M7.2 earthquake. Roberts et al. (2013) reported a landslide-generated impulse
70 wave in Chehalis Lake, Canada in December 2007 due to the failure of a 3 million m^3 rockmass. Some
71 other similar destructive incidents include: Pontesei dam (Italy) incident in 1959 (Panizzo et al. 2005),
72 Three Gorges Reservoir (China) incidents in 2003, 2008 and 2015 (Huang et al., 2012; Yin et al. 2015;
73 Zhou et al. 2016); the 2008 San Juan de Grijalva landslide (Alcantara-Ayala and Dominguez-Morales,
74 2008); and Lake Lucerne in Switzerland in June 2007 (Evers et al., 2019a). Hermanns et al. (2014)
75 and Roberts et al. (2014) provided reviews of regional and global incidents, respectively. An important
76 aspect of the landslide-generated waves in the Apporo dam reservoir is the occurrence of multiple
77 landslides, which potentially increases hazard magnitude. Other worldwide incidents of multiple
78 landslides in a dam reservoir or fjord are the 2007 Aysen Fjord, Chile (Oppikofer et al., 2019), the
79 2018 Palu event within the Palu bay, Indonesia (Takagi et al., 2019; Heidarzadeh et al., 2019), and the
80 1964 incident in Kenai Lake, Alaska (USA) (McCulloch, 1966). The Indonesian event involved both
81 subaerial and submarine landslides.

82 In this study, we report results of our field surveys of the evidence of landslide-generated waves in
83 the Apporo dam reservoir following the September 2018 Hokkaido earthquake. In order to contribute
84 to the safety of dams worldwide, it is critically important to report and analyze any incident of

landslide-generated waves in dam reservoirs. The authors visited the Apporo dam area in the period 29 May – 4 June 2019 to conduct field surveys of the landslide-generated waves. Here, we report our field survey results, analyze them, and compare the measured landslide-generated wave runup height with those obtained using existing empirical equations.

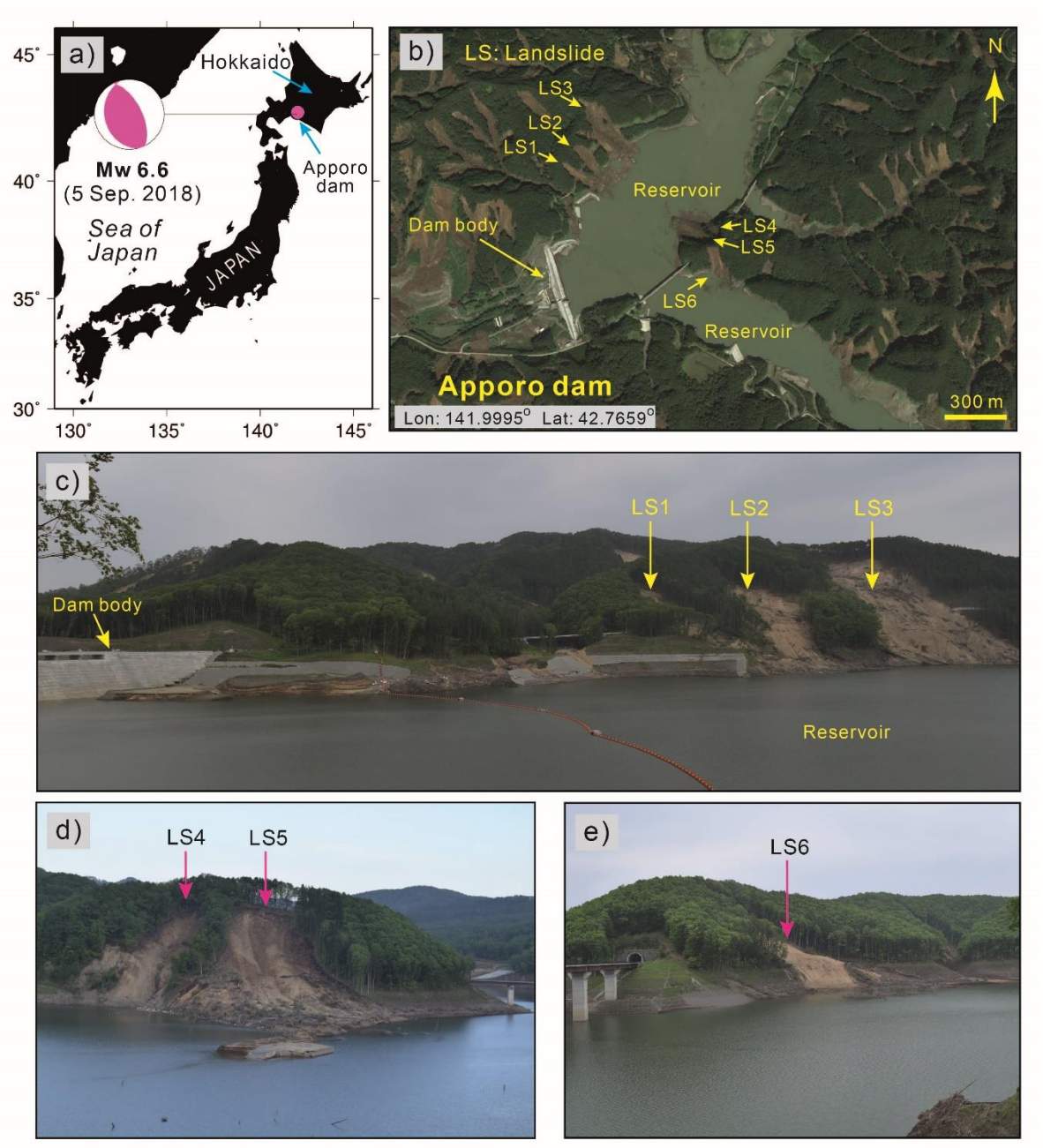

Figure 1. a) Location of the Apporo dam and reservoir in Hokkaido, Japan and the epicenter of the

earthquake. **b)** A satellite image from Google-Earth (https://earth.google.com/) showing the dam area after the earthquake and the location of six landslides (LS1 – LS6) near the dam body. **c), d), e)** Our field photos showing detailed views from the six landslides near the dam body. LS is an acronym for "landslide".

2. Background information

2.1 Apporo dam in Hokkaido, Japan

Apporo dam is a trapezoidal Cemented Sand and Gravel (CSG) dam located in Hokkaido (Figures 1-2), which was built for flood control and supplies water for irrigation and domestic uses. The dam construction was completed in 2019. The CSG dam is a relatively new type of dam construction technology, which was developed in Japan and offers benefits such as its environment-friendly construction materials, higher dam stabilities and low maintenance costs (Japan Commission on Large Dams, 2018). In principle, a CSG dam is a type of gravity dam that comprises a trapezoid body filled with CSG materials, which are relatively cheap and can be rapidly constructed with relatively simple technologies. The dam body is protected by a concrete layer at its face on all sides with a thickness of 1.5 m (Figure 2b). The Apporo dam has a height of 47.2 m, a crest length of 516 m, a dam body volume of 480,000 m^3, reservoir water volume of 47.4 million m^3, and reservoir surface area of 3.03 million m^2 (Japan Commission on Large Dams 2018). The dam is equipped with an Ogee-type spillway (e.g., Savage and Johnson, 2001) fitted in the middle of the dam body (Figure 2a and 2d). The CSG material used for the dam body is shale and the dam foundation is made of alternate layers of

111 shale and shale-sandstone.

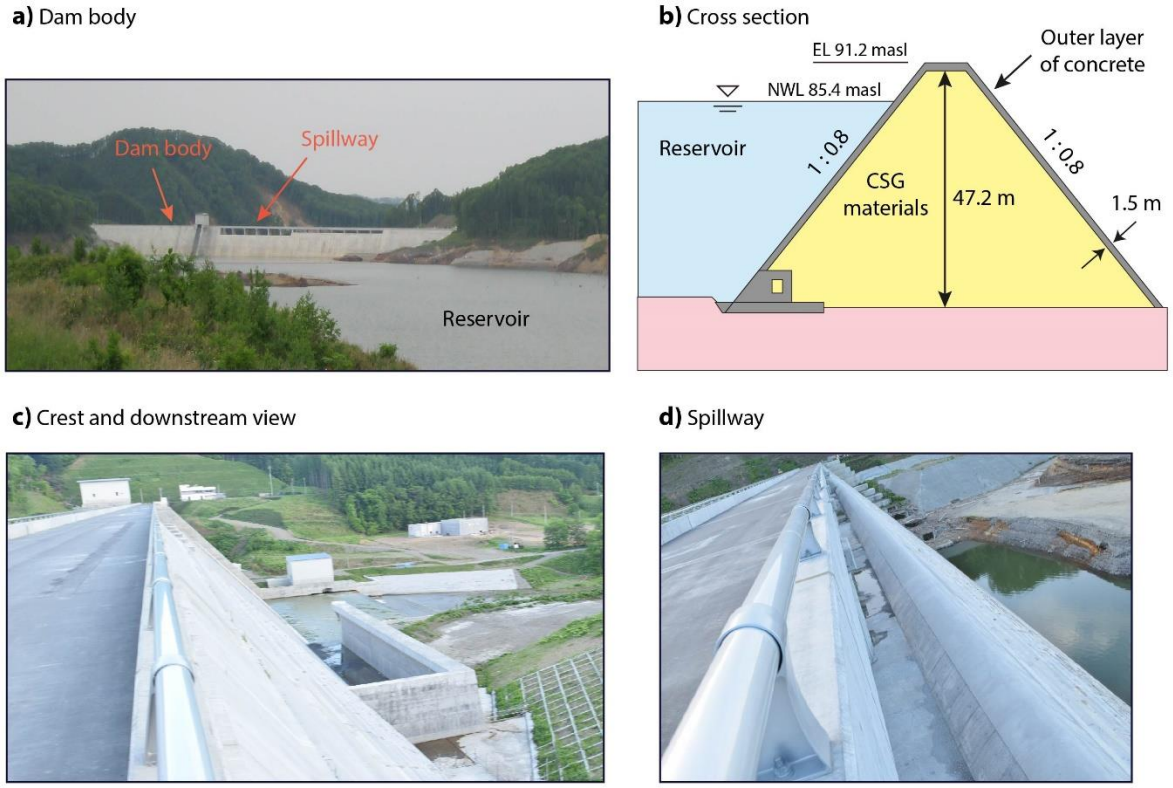

112

113 **Figure 2.** Apporo dam located in Hokkaido, Japan. **a)** A field photo showing the dam body and the
114 reservoir. **b)** A cross-section of the dam showing that the dam is constructed from Cemented
115 Sand and Gravel (CSG) with a 1.5 m concrete layer at the outer layer. This sketch is based on
116 the dam body drawings provided to the first author by the site engineers during the surveys. **c)** A
117 view of the dam crest and the downstream area. **d)** The entrance of the spillway. In panel "b",
118 EL, NWL and masl are abbreviations for "Elevation", "Normal Water Level", and "meters
119 above the sea level", respectively.

120

121 **2.2. Interactions of the September 2018 typhoon Jebi and Hokkaido earthquake**

122 The purpose of this section is to add insights into the origin of extraordinary landslide activities in
123 the Atsuma area through analyzing earthquake and typhon data and their timings. The data used for

this analysis are the earthquake mainshock and aftershock information, the rainfall data, and typhoon pressure field. Earthquake data belong to a period of one month after the mainshock (i.e., 5 September – 5 October 2018) and are provided by the unified earthquake catalogue of Japan Meteorological Agency (https://www.data.jma.go.jp/svd/eqev/data/bulletin/hypo.html). For earthquake focal mechanisms, we used the focal mechanism catalogue of the Global Centroid Moment Tensor (GCMT) project (Dziewonski et al. 1981; Ekström et al. 2012). The data of rainfall and typhoon pressure field are from the Automated Meteorological Data Acquisition System (AMeDAS) of the Japan Meteorological Agency (https://www.jma.go.jp/jma/en/Activities/amedas/amedas.html).

Rainfall and Typhoon Jebi's pressure field are shown in Figure 3. Typhoons that make landfall in Japan usually rapidly lose their energy and become tropical depressions, but Typhoon Jebi maintained a typhoon-status intensity with its central pressure of 975 hPa (hectopascal) and maximum wind speed of 50 knots (25.7 m/s) when it approached Hokkaido (Figure 3b). This caused a band of heavy rainfall along the path of the typhoon (Figure 3c). The rainfall in this area was relatively heavy from June to September 2018. Since the event occurred in the summertime with hot weather and sunny days, the surfaces of the mountain tended to be dry, but the deeper part (deeper than 10-20 cm) of the ground is assumed to be wet. In addition, Typhoon Jebi caused heavy rainfall in the vicinity of Atsuma. In particular, Typhoon Jebi's daily rainfall was 12-14 mm in the Atsuma region immediately before the earthquake (arrows in Figure 3a), which most likely was sufficient to entirely saturate the mountains and make them susceptible to sliding.

143 The distribution of aftershocks of the earthquake (Figure 4a) shows that the Apporo dam is located
144 within the intensive aftershock activity zone. The total length of the intensive aftershock zone is
145 approximately 32 km which begins from around the coastline (latitude 42.55°) and extends to the north
146 until approximately latitude 42.83°. The dam is located approximately 9 km to the north of the
147 mainshock epicenter (Figure 4a). Detailed analyses from the relocated aftershocks by using data from
148 a permanent local seismic network revealed that the aftershock depths were concentrated at the depth
149 of 20-40 km (Katsumata et al., 2019). Magnitude-time distribution of the aftershocks and their
150 cumulative number (Figure 4b) show steady growth of aftershocks during the 30 days following the
151 mainshock.
152 Among other factors, landslides occur following heavy rainfall, such as many landslides that
153 occurred in Dominica following the 2017 Hurricane Maria (Heidarzadeh et al. 2018), or following
154 ground shaking induced by earthquakes, such as landslide activities in Palu (Indonesia) following the
155 September 2018 earthquake (Takagi et al. 2019) and other events (e.g., Heidarzadeh and Satake, 2015;
156 Tsuji et al., 2011). The landslides in the Atsuma region in September 2018 occurred due to the
157 combined effects of typhoon rainfall and earthquake shaking. Although it is a challenge to precisely
158 quantify the contribution of each trigger to landslide initiation, the extraordinary landslide occurrences
159 in the region can be explained by the combined effects of the earthquake and the typhoon. Such
160 destructive hazard combinations and interactions were discussed by several authors (e.g., Gill and
161 Malamud 2016; Liu et al. 2016; Lyddon et al. 2019; Adams and Heidarzadeh 2021). Gill and Malamud

(2016) presented three types of relationships among interacting hazards which are: increased probability, triggering, and catalysis (i.e., wet soils due to heavy rainfall at the time of the earthquake increased the number and extent of landslides). For the case of the 2018 Atsuma landslide incident, the two primary hazards (i.e., the earthquake and the typhoon) are completely independent and neither of them was the triggering mechanism for the other. However, they worked together to trigger a secondary hazard (i.e., the landslides), increased landslide probability and catalyzed it. In fact, the 2018 Atsuma landslide disaster, with 36 deaths, is a rare case that involves all three mechanisms (i.e., increased probability, triggering, and catalysis).

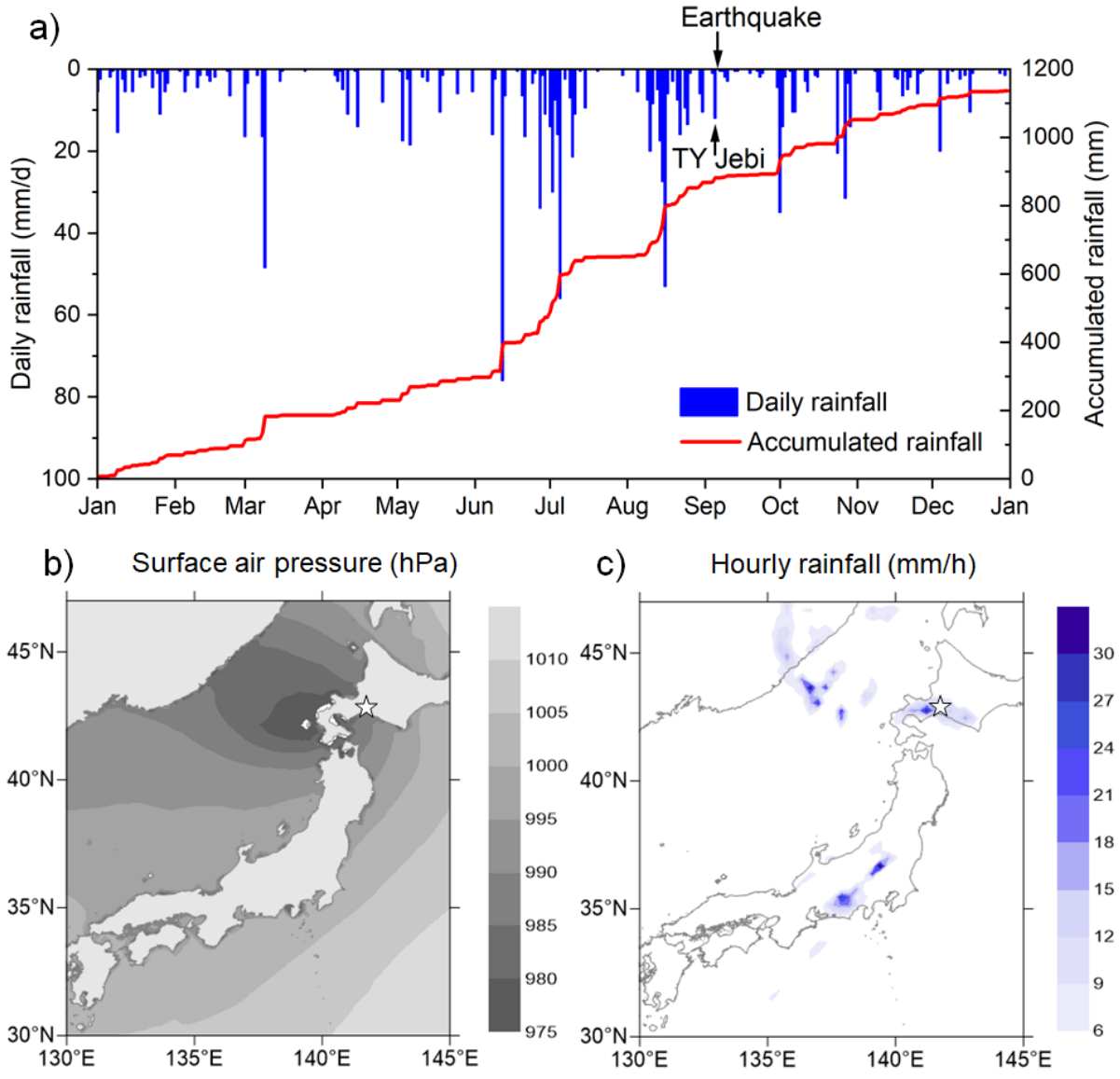

Figure 3. a) Rainfall records at Atsuma meteorological station operated by JMA spanning 2018. The times of the earthquake and Typhoon Jebi are marked in the figure by arrows. **b)** Surface air pressure at the time of Typhoon Jebi's approach to Hokkaido (17:00 UTC on 4 September 2018). **c)** Rain band induced by the Typhoon Jebi. The stars in panels “b” and “c” indicate the location of Atsuma Town. Surface air pressure and rainfall data are extracted using the typhoon model with the meso-scale weather forecasting model of the Japan Meteorological Agency (JMA-MSM) (Takagi and Takahashi 2021).

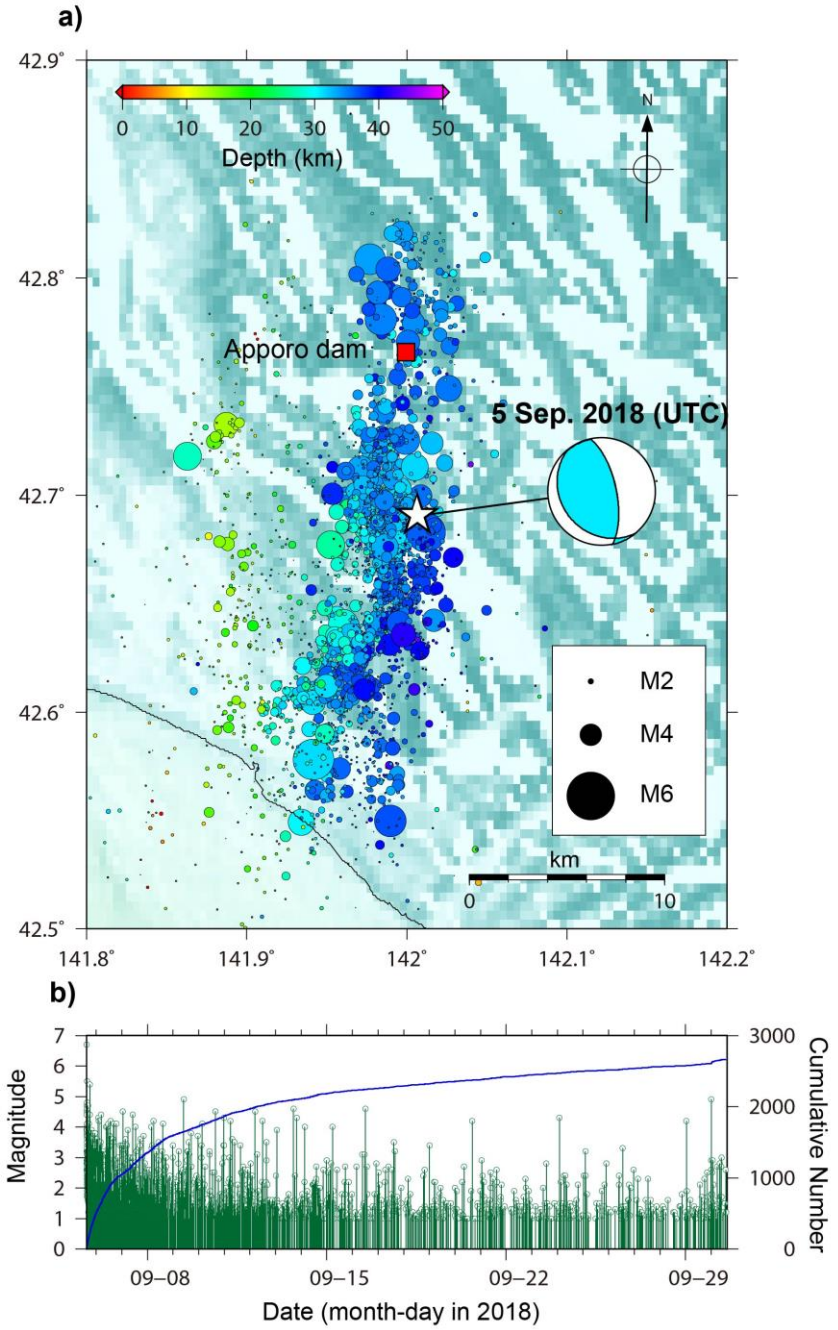

181

182 **Figure 4.** The mainshock and one-month aftershocks (M1 or larger) of the 5 September 2018

183 Hokkaido M_w 6.6 earthquake around the Apporo dam. **a)** Distribution of the one-month

184 aftershocks and the mainshock in the region relative to the dam site. **b)** Magnitude-time plot

185 indicated by the left vertical axis and the green bars and circles. The right vertical axis and the

186 thick blue curve indicate the cumulative number of aftershocks. The horizontal axis begins from

187 the earthquake origin time (i.e., 5 September 2018 UTC). Star shows the epicenter of the

188 earthquake.

189

190 **2.3. Landslide activities following the typhoon Jebi and Hokkaido earthquake**

191 Landslide activity and characteristics following the September 2018 Hokkaido earthquake have
192 been studied by several authors. According to Yamagishi and Yamazaki (2018), the geology of the area
193 is Neogene sedimentary rocks covered by air-fall lapilli-sized pumice (9000 years ago) with maximum
194 surface thickness of 4-5 m. Yamagishi and Yamazaki (2018) found that the majority of the landslides
195 were shallow planar landslides, with a few meters of depth, and they initiated within the pumice layer.
196 During our field surveys, we also observed that most of the landslides around the Atsuma area were
197 shallow with an average depth of approximately 2-3 m (Figure 5). Satellite data analyses by Aimaiti et
198 al. (2019) provided a tool to map the co-seismic landslides. Zhang et al. (2019) reported that most of
199 the landslides occurred in areas with Modified Mercalli Intensity of 7-8 with peak ground acceleration
200 in the range from $0.4g$ to $0.7g$, where g is gravitational acceleration (= 9.81 m/s^2). The slope angles
201 of the landslides were between 15° and 35° (Zhang et al. 2019). According to Osanai et al. (2019),
202 some large-scale and deep-seated landslides also were generated, including a landslide that formed a
203 landslide dam in the area. Wang et al. (2019) identified 7,837 landslides with a total volume of 23–38
204 million m^3 of deposits. Other authors who studied this event include Li et al. (2020), Chang et al.
205 (2021), Chen et al. (2021) and Lu et al. (2021).

206

Figure 5. Field survey photos of landslides following the September 2018 earthquake around the Atsuma area of Hokkaido (Japan). **a)** A shallow landslide near a road. **b)** and **c)** A water treatment plant destroyed by a landslide on a nearby slope. **d)** A shallow landslide near a road. **e)** A narrow and shallow landslide. **f)** A large shallow landslide.

214 **3. Data and methods**

215 The records of reservoir water level and reservoir water volumes are provided by the Hokkaido
216 Prefecture Dam Authority. The time interval of reservoir water level measurements is 10 min. Field
217 data are collected during our fieldworks in the affected area (Hokkaido, Japan). The authors surveyed
218 the Atsuma area, including the Apporo dam site, for field surveys. During the fieldwork, we measured
219 landslide dimensions (i.e., length, width, thickness, elevation) and the runup height of the
220 landslide-generated waves using a TruPulse 200 laser rangefinder (Laser Technologies Inc) (Figure 6).
221 The sites of the measurements were located by a handheld GPS device of the Garmin model (Garmin
222 Ltd.) for georeferencing the locations. All locations were photographed, and notes were made. The
223 measured value of wave runup height was corrected relative to the reservoir water level at the time of
224 the event (Fritz et al. 2008; Omira et al. 2019; Heidarzadeh et al. 2018, 2020). The reservoir water
225 level at the time of our survey (4 June 2019) was 68.9 masl (meters above the sea level) whereas it
226 was 70.8 masl at the time of the event (5 September 2018; UTC) (Figure 7). The dimensions of the
227 landslides were used to approximate the volume of the landslides using simple mathematical equations
228 for the volume of geometrical shapes.

229 We compared the measured runup height of the landslide-generated waves with those obtained
230 using existing empirical equations. The motivation for conducting this comparison was to examine the
231 reproducibility of the field-measured runup height measurements using existing empirical equations
232 and to encourage further research on developing such empirical equations.

4. Field survey results

We identified six landslides in the vicinity of the dam body through our fieldwork (LS1 to LS6 in Figures 1 and 6). A summary of landslide dimensions and their volume estimates are presented in Table 1. As previously reported by other authors (e.g., Yamagishi and Yamazaki 2018), most of the landslides in the Atsuma region triggered by the 2018 earthquake were shallow. Our measurements showed that the maximum thicknesses of the landslides were 2-3 m (Figure 6b). Among the six landslides, the largest landslide is LS3 (Figure 6e,f) with a length and maximum width of 330 m and 140 m, respectively. The volume of LS3 is estimated at 71.4×10^3 m^3 (Table 1). The landslides displaced the vegetation and tall trees into the reservoir water (Figures 1, 6). Debris were found at the other side of the reservoir at the location of wave runup measurement (Figure 8).

The large amount of displaced soil and vegetation/trees into the reservoir water caused a rapid raise in the reservoir water level (Figure 7). Immediately after the earthquake occurrence, the reservoir water level started to raise and increased from 70.8 masl to 71.1 masl (i.e., 0.3 m increase of water level) within approximately 60 min from the earthquake origin time (Figure 7). The reservoir water volume raised by 0.38 million m^3 based on the recorded rise in the reservoir water level. Although reservoir water volume changes provide important data on the intrusion of landslide materials into the reservoir, it is a challenge to solely associate the water volume raise to the landslides because the reservoir was constantly fed by the river and floods at the time of the incident and there were other coincident landslides in the reservoir far from the dam body. Table 1 shows that the total volume of all

six landslides (LS1 – LS6) is approximately 0.19 million m^3 (i.e., 190.7×10^3 m^3), which is around half of the reservoir water volume increase.

Data from our surveys revealed that the intrusion of the subaerial landslides into the reservoir was associated with landslide-generated waves in the reservoir. A clear sign of such waves was observed at a narrow opening of the reservoir around the left abutment of the dam (Figures 8, 9). At this location, we observed a chaotic pile of woody debris (Figure 8) and damage to the concrete revetment (Figure 9). The damage to the concrete revetment can be possible only by powerful waves. This observation was confirmed through discussions with site engineers during our surveys who verified that such damage to the revetment and the tree debris was non-existent before the earthquake. Due to the relatively long sampling interval of reservoir water level measurements (i.e., 10 min), it is not possible to see traces of transient water waves generated by the landslides as such waves normally have a wave period of less than 1 min or up to a few minutes for the potential consequent oscillations for large reservoirs. Figure 7 confirms that such transient water waves or potential consequent oscillations are not recorded due to the long sampling interval of the water level data. As compared to other similar incidents worldwide, such landslide-generated wave damage and high-water marks were reported, for example, during the 2007 landslide-generated waves in Chehalis Lake (Canada) as reported by Roberts et al. (2013).

We measured the runup height generated by the landslide-generated waves (parameter 'R' in Figure 8) as 5.3 m. The inundation distance at this location was ~80 m. Among the six landslides

identified in the vicinity of the dam body, it is likely that only three of them, i.e., LS1, LS2 and LS3, contributed to the wave runup measured at the left abutment of the dam, given the locations of the landslides and the potential propagation paths of the waves. The precise location of the runup measurement point is indicated in the inset of Figure 8a,b. This runup measurement is only for one single location at the banks of the reservoir and cannot be generalized for other locations. For example, we were unable to measure the runup of landslide-generated waves on the dam body as watermarks were not available on the dam body. However, it would be fair to assume that the wave runups on other locations in the reservoir were of the same order of magnitude (i.e., R = 1 – 10 m) (e.g., Muhari et al., 2019). Therefore, we may conclude that although the landslide-generated waves made some damage to the reservoir banks, they were not a major risk for the safety of the dam as the reservoir water level was approximately 20 m below the dam crest elevation at the time of the earthquake (Figure 7).

284

285 **Figure 6. a)** Characteristics and dimension estimates of landslides LS1, LS2 and LS3. The background

286 satellite image in panel "a" is from Google-Earth satellite images (https://earth.google.com/) but

287 the dimensions are based on our field surveys. **b), c), d), e), f)** Our field photos of the landslides

288 from our surveys.

289

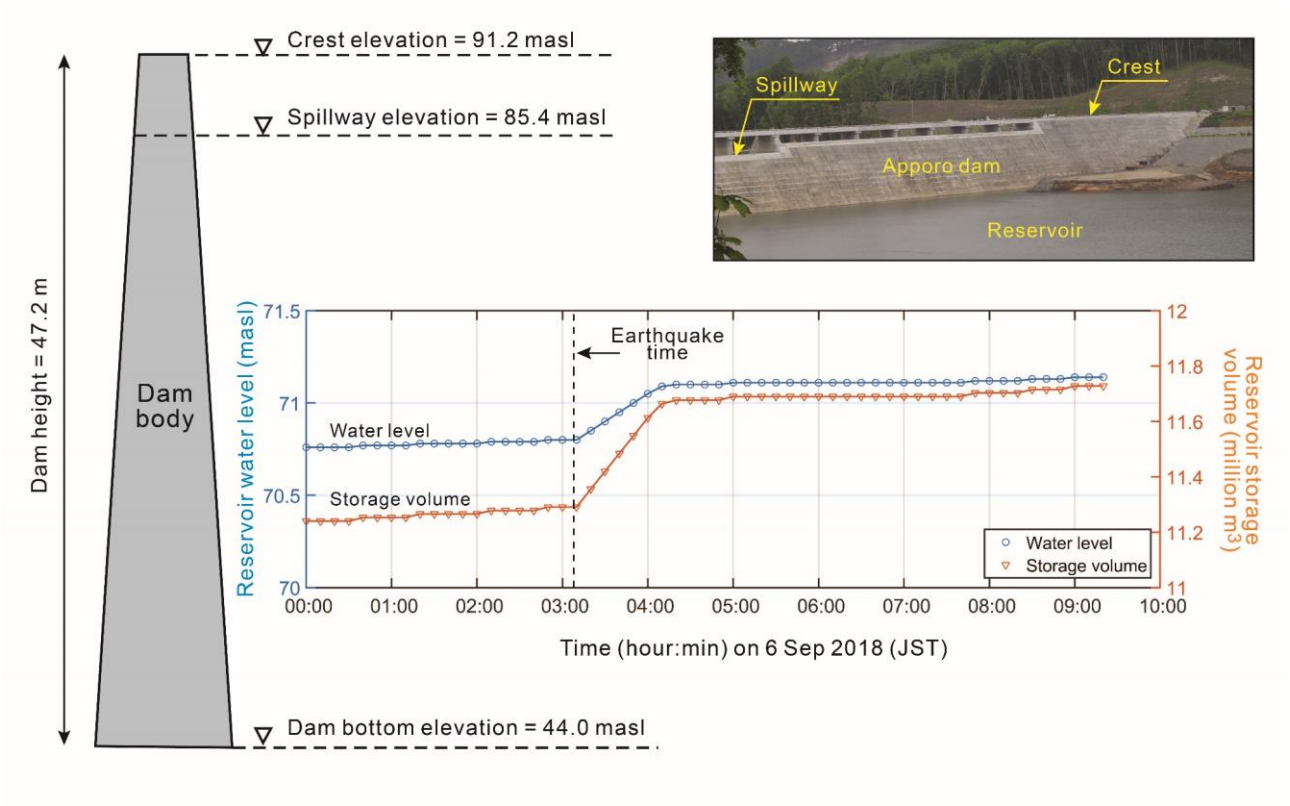

290

291 **Figure 7.** Temporal variations of reservoir water level (blue) and reservoir storage volume (orange)

292 during the 2018 earthquake and consequent landslides. The vertical dashed line shows the origin

293 time of the earthquake. JST stands for Japan Standard Time. The term 'masl' represents 'meters

294 above the sea level'.

295

296

297

298

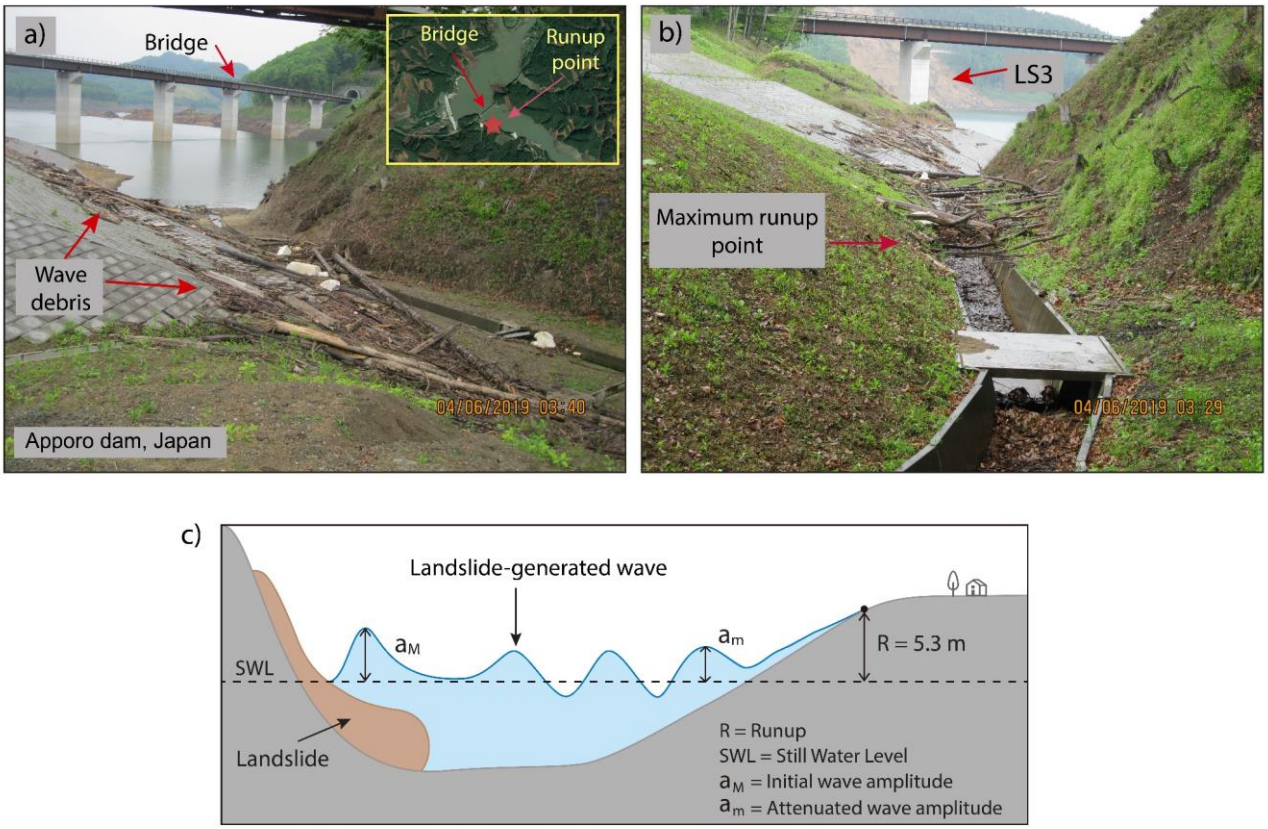

299

300 **Figure 8.** Measurement of the runup of the landslide-generated waves in the Apporo dam reservoir
301 following the September 2018 Hokkaido earthquake. **a), b)** Runup measurement point showing the
302 debris generated by landslide-generated wave. The inset at the upper-left of panel "a" shows the
303 runup measurement point. **c)** Sketch showing the definition of maximum initial wave amplitude
304 (a_M), the attenuated wave amplitude due to propagation (a_m), and runup height (R).

305

306

307

308

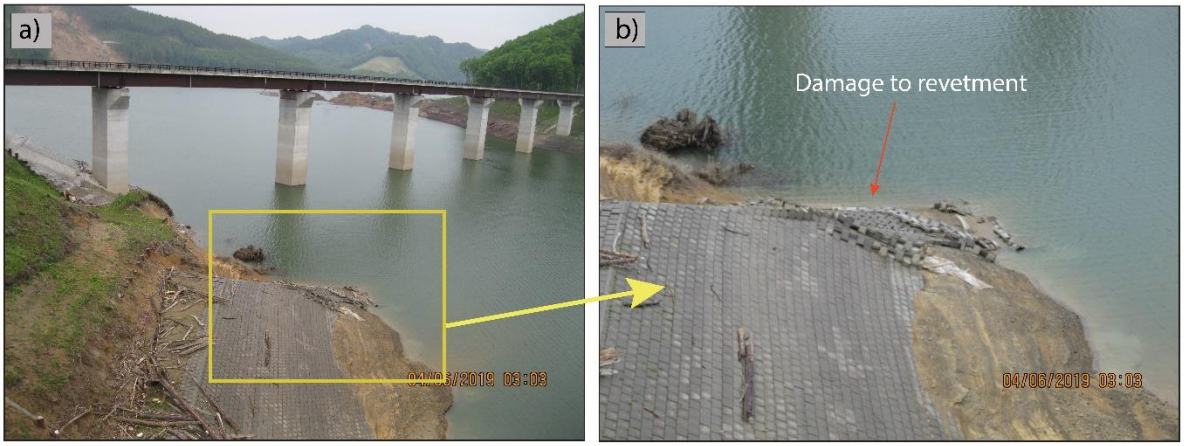

Figure 9. Damage from the landslide-generated waves around the left bank of the Apporo dam reservoir following the September 2018 Hokkaido earthquake. This is the entrance of the opening that we measured runup (Figure 8). **a)** A photo from far showing the damaged reservoir bank revetment, the reservoir and the bridge passing through the reservoir. The box indicates the area enlarged in panel "b" of this figure. **b)** A close-up view of the damaged area, which is the area shown in a box in panel "a".

Table 1. Estimated dimensions and volumes of landslides. See Figures 1 and 6 for the locations of the landslides. All of these six landslides entered the reservoir, but it is speculated that only three of them (LS1, LS2 and LS3) were responsible for the observed runup.

Name of landslide	Slide length ($\boldsymbol{l_s}$), m	Slide width ($\boldsymbol{b_s}$), m	Maximum slide thickness ($\boldsymbol{s_{max}}$), m	Slide volume ($\boldsymbol{V_s}$), m^3	Slope angle ($\boldsymbol{\alpha}$), ^{o}	Drop heights (Δz), m	Included in wave estimation?
LS1	205	55	2.5	23.3×10^3	20	128	Yes
LS2	200	70	2.5	28.2×10^3	20	104	Yes
LS3	330	140	2.5	71.4×10^3	20	85	Yes
LS4	115	40	2.5	9.7×10^3	20	80	No
LS5	235	75	2.5	35.0×10^3	20	95	No
LS6	175	65	2.5	23.1×10^3	20	65	No
Total				190.7×10^3			

5. Estimating runup heights using empirical equations

It is known that the process of estimating landslide-generated waves using empirical equations is associated with uncertainties. Sabeti and Heidarzadeh (2020) showed that the maximum initial wave amplitude predictions differ up to thousands of times from one empirical equation to another, although they studied only waves generated by submarine landslides. Despite this, it is useful to apply such empirical equations in order to examine their performance and encourage new research on the improvements of such empirical equations.

In this section, we work with three wave parameters: the maximum initial wave amplitude generated by the subaerial landslide (a_M; Figure 8c), the attenuated wave amplitude due to propagation (a_m; Figure 8c), and the wave runup height on the reservoir banks (R; Figure 8c). To estimate a_M, we apply eight independent empirical equations proposed by Fritz et al. (2004), Xue et al. (2019), Heller and Hager (2014), Heller and Spinneken (2015), Slingerland and Voight (1982), Ataei-Ashtiani and Nik-Khah (2008), Noda (1970) and Mohammed and Fritz (2012). There are other equations such as those proposed by Heller and Hager (2010) and McFall and Fritz (2016). It is noted that these equations are a mix of those generated through 2D (e.g., Fritz et al., 2004) and 3D experiments (e.g., Mohammed and Fritz, 2012). Some studies have shown that the experiments conducted in 2D may overestimate the wave amplitudes (e.g., Heller and Spinneken, 2015).

For runup calculations (R), we applied two independent equations by Synolakis (1987) and Evers and Boes (2019), which are obtained through independent physical experiments. Attenuation of the

339 wave due to propagation is considered using the equation proposed by Fritz et al. (2004) by assuming
340 weakly nonlinear oscillatory wave region. The attenuated wave amplitude due to propagation is called
341 a_m here (Figure 8c, Table 2). For these calculations, we considered the three slides LS1, LS2 and LS3
342 because potential waves generated by the other three slides were mostly directed outside of the runup
343 measurement point due to their locations. For inputting landslide parameters into the empirical
344 equations, it is assumed that the three landslides LS1, LS2 and LS3 form a combined large landslide
345 and occurred simultaneously although we do not have information about the timing of these landslides.
346 We assumed that the total volume of all landslides contributed to wave generation although it might be
347 the case that some small part of landslide materials might not have entered water. The water depth (h)
348 and slope angle (α) are considered as 27.0 m and 20°, respectively, for all slides in this study.
349 The results of predictions for maximum initial wave amplitude (a_M), attenuated wave amplitude
350 due to propagation (a_m), and runup height (R_1 and R_2) are presented in Table 2 indicating that the
351 equations result in runup values in a wide range of 1.3 – 98.2 m, whereas the measured runup in the
352 field was 5.3 m. Among the examined empirical equations, those of Xue et al. (2019) and Heller and
353 Hager (2014) give the closest predictions to the measured runup, with respective runup predictions of
354 7.2 m and 6.2 m, respectively. Some equations, such as Noda (1970), result in extreme overestimation,
355 such as 98.2 m, which are far greater than the actual measurement. This could be partly because some
356 of the equations used in Table 2 are based on 2D experiments, which are thought to overestimate the
357 waves. It is useful to note that the two equations that we applied for runup predictions (Synolakis

1987; Evers and Boes, 2019) yield values close to one another although that of Evers and Boes (2019) predicts slightly higher. We note that the actual wave runup process is associated with 3D effects which implies that the wave propagates in various directions and undergoes transformation while propagating over irregular bathymetry. These phenomena introduce further challenges for applying empirical equations.

The analysis of wave prediction using existing empirical equations reveals that the measured runup height of 5.3 m (Figure 8c) can be approximately reproduced by two equations of Xue et al. (2019) and Heller and Hager (2014) whereas other predictive equations are unsuccessful in reproducing the field measurement.

Table 2. The maximum initial wave amplitude (a_M), the attenuated wave amplitude due to propagation (a_m), and runup height (R_1 and R_2) estimated from various empirical equations for the combination of three landsides of LS1, LS2, and LS3. The average value of drop heights for LS1, LS2 and LS3 is used for calculations.

Empirical equations*	Landslide parameters**		$\boldsymbol{a_M}$, (m)	$\boldsymbol{a_m}$, (m)$^{+}$	$\boldsymbol{R_1}$, (m)$^{++}$	$\boldsymbol{R_2}$, (m)$^{\#}$
	l_s, (m)	b_s, (m)				
$\frac{a_M}{h} = 0.25\left(\frac{v_s}{\sqrt{gh}}\right)^{1.4}\left(\frac{s}{h}\right)^{0.8}$	245.0	265.0	2.0	0.6	1.5	1.8
$\frac{a_M}{h} = 0.40\left(\frac{v_s}{\sqrt{gh}}\right)^{0.81}(s/h)^{0.40}(l_s/h)^{0.18}tan^{0.15}\alpha$	245.0	265.0	7.9	2.3	8.2	7.2
$\frac{a_M}{h} = \frac{4}{9}\left[\frac{v_s}{\sqrt{gh}}\left(\frac{s}{h}\right)^{0.5}\left(\frac{m_s}{\rho_w b_s h^2}\right)^{0.25}(\cos\frac{6}{7}\alpha)^{0.5}\right]^{0.8}$	245.0	265.0	6.8	1.9	6.7	6.2

$\frac{a_M}{h} = 0.50\left[\left(\frac{v_s}{\sqrt{gh}}\right)^{1.00}\left(\frac{s}{h}\right)^{1.10}\left(\frac{m_s}{\rho_w b_s h^2}\right)^{1.00}\right]^{0.85}$	245.0	265.0	2.4	0.7	1.8	2.1
$\frac{a_M}{h} = 10^{\left[-1.25+0.71\log\left(0.5\,\frac{\rho_s}{\rho_w}\frac{V_s}{h^3}\frac{v_s^2}{gh}\right)\right]}$	245.0	265.0	39.5	11.2	60.8	41.2
$\frac{a_M}{h} = \left[0.398+0.076\left(V\left(\frac{v_s}{\sqrt{gh}}\right)^2\right)^{1.27}\right](\frac{T_s}{V})^{-0.26}(\frac{l_s}{s})^{-0.125}(\frac{r}{h})^{-0.48}$	245.0	265.0	11.4	Included	62.2	42.1
$\frac{a_M}{h} = 1.32(\frac{v_s}{\sqrt{gh}})$	245.0	265.0	58.0	16.5	98.2	65.3
$\frac{a_M}{h} = 0.31\left(\frac{v_s}{\sqrt{gh}}\right)^{2.1}\left(\frac{s}{h}\right)^{0.6}\cos\theta\,(\frac{r}{h})^{n}$	245.0	265.0	0.5	Included	1.3	1.6

*: Developers of the equations are Fritz et al. (2004), Xue et al. (2019), Heller and Hager (2014), Heller and Spinneken (2015), Slingerland and Voight (1982), Ataie-Ashtiani and Nik-Khah (2008), Noda (1970) and Mohammed and Fritz (2012) for the first, second, third, fourth, fifth, sixth, seventh and eighth, equations, respectively.

**: a_M, the maximum initial wave amplitude; a_m, the attenuated wave amplitude due to propagation; R_1 and R_2, and runup height; l_s, average length of three landslides of LS1, LS2, and LS3; b_s, sum of the width of three landslide (LS1, LS2, LS3); h, water depth (h = 27 m in this study); $v_s = \sqrt{2g\Delta z(1-\tan\delta\cot\alpha)}$, slide velocity at impact; Δz (= 85 m), the drop height between the location of the slide centroid at rest and slide centroid reaching the initial water level; g, gravitational acceleration; δ (= 26°), dynamic bed friction angle; α, slope angle of landslide (α = 20° in this study); s, slide thickness; l_s, slide length; m_s, slide mass; ρ_w (=1000 kg/m^3), water density; ρ_s (=1700 kg/m^3), slide density; r(=650 m), distance between the location of wave runup and impact point; θ (=10°), direction relative to landslide propagation; $T_s = 0.43V^{-0.27}\frac{v_s}{\sqrt{gh}}^{-0.66}(\sin\alpha)^{1.32}$ is the dimensionless slide underwater travel time; $V = V_s/b_s h^2$, dimensionless slide volume Equation for v_s is from Kamphuis and Bowering (1970); $n = -1.2\left(\frac{v_s}{\sqrt{gh}}\right)^{0.25}\left(\frac{s}{h}\right)^{-0.02}\left(\frac{b_s}{h}\right)^{-0.33}$, based on Mohammed and Fritz (2012).

+: For estimating attenuation of the waves due to propagation, we used the equation by Fritz et al. (2004): $\frac{a_m}{a_M} = \left[1+\frac{(x_M-r)}{h}\right]^{-0.4}$, where, a_m is the attenuated maximum positive wave amplitude due to a propagation distance of r, x_M (=50 m) is the location of the maximum initial wave amplitude, and r (= 650 m) is the propagation distance.

++: Runup equation based on Synolakis (1987): $R_1 = 2.831\,h\,(\cot\beta)^{0.5}\,(a_m/h)^{1.25}$, where R_1 is runup, β is beach slope (β = 10° in this study), and a_m is the attenuated maximum positive wave amplitude due to propagation.

#: Runup equation based on Evers and Boes (2019): $R_2 = 2\,a_m\,e^{0.4\,(\frac{a_m}{h})}\,(\frac{90^\circ}{\beta})^{0.2}$, where R_2 is runup, β = 10° in

this study, and a_m is the attenuated maximum positive wave amplitude due to propagation..

6. Discussions

The predictions of wave runup made by various existing empirical equations are divided by a couple of orders of magnitude (up to approximately hundred times) (Table 2). However, this is not a surprise because most empirical relationships are developed using limited laboratory data which are obtained under various limitations (e.g., Sabeti and Heidarzadeh 2020). Several reasons may contribute to such large uncertainties associated with the prediction of empirical equations, such as: (i) lack of enough experimental database that could include a large number of data points (e.g., 1000s of data points); (ii) the rather complicated mechanism of wave generation process by landslides which involves many factors such as water depth, type of the sliding materials, friction, rheology, speed and other factors; (iii) lack of enough actual field data that could help to further constrain empirical equations and improve their predictions as actual field data with real measurements are very limited, (iv) experimental studies are conducted in small lab scales which are subject to various scale and model effects (e.g., Heller et al., 2008), and (v) propagation of the wave over actual irregular bathymetries, which are not properly represented by empirical predictive equations (e.g., Franco et al., 2021). Therefore, efforts in various fronts need to be made to further improve the qualities of predictive relationships including additional experimental and field data. Our field data from the Apporo dam landslide-generated waves could provide data for improving the qualities of empirical equations in the future.

Landslide-generated waves are real threats to dams' safety worldwide and must be taken seriously. They can endanger the safety of dams and the surrounding communities as evidenced by the Vajont dam disaster (Italy) in 1963 (Barla and Paronuzzi, 2013; Roberts et al., 2014). In particular, even moderate-size landslides could be of high safety risks for situations when the reservoir water level is closer to the dam crest elevation. Therefore, although the 2018 Apporo dam landslide-generated wave did not make large destruction or overtopping as the reservoir water level was significantly lower than the normal water level at the time of the event, it must be considered as a warning call for the dam authorities to carefully assess unstable slopes around the dam reservoir, estimate their potential sizes, prepare emergency guidelines in case of slope failures, and consider stabilization works on the unstable slopes as much as possible. It is possible that a larger-magnitude earthquake could trigger a much larger landslide with more severe consequences.

7. Conclusions

The destructive and rare combination of the September 2018 Typhoon Jebi and M_w 6.6 Hokkaido Earthquake led to the generation of nearly 6,000 landslides in Hokkaido (Japan), where several of them slid into the Apporo dam reservoir and produced landslide-generated waves. We conducted field surveys of the landslides around the Apporo dam and documented six landslides in the vicinity of the dam body. The largest of these landslides has a length and maximum width of 330 m and 140 m, respectively, with an estimated volume of 71,400 m^3. We identified impacts of a landslide-generated

wave around the left abutment of the dam which caused some damage to the concrete revetment. The surveyed runup height of this wave was 5.3 m, which was reproduced employing two independent empirical equations and using landslide parameters although we acknowledge that such applications of empirical predictive equations are associated with uncertainties. By considering the locations of the landslides and their potential propagation paths, we speculate that possibly three of them contributed to the measured wave runup. This landslide-generated wave was not a major risk for the dam's safety, but it could have had serious consequences if the reservoir water level was closer to the dam crest elevation or if the size of the landslides was larger. Although two independent empirical equations successfully reproduced our surveyed runup, some others failed which can be attributed to the large uncertainties associated with predictions made by empirical equations. The field-measured data provided in this research can be used to improve the quality of predictions made by empirical equations. Our field data also serves as a call for strengthening safety of dams to landslide-generated waves in reservoirs.

Acknowledgements

A number of figures were drafted using the GMT software (Wessel and Smith 1998). We thank the engineers at the Apporo dam (Hokkaido, Japan) for assisting us during the field surveys and the Hokkaido Prefecture Authorities for providing reservoir water level data. We are grateful to the Editor, one anonymous reviewer, and Dr Nicholas J. Roberts for their constructive and useful review

comments.

Funding

This research is funded by the Great Britain Sasakawa Foundation (http://www.gbsf.org.uk/) under grant number 5542 (2018), and the Royal Society, the United Kingdom, grant number CHL/R1/180173. We also acknowledge funding from the open funding of State Key Lab of Hydraulics and Mountain River Engineering, Sichuan University, grant number SKHL2101.

Availability of data and materials

All data used in this research are provided in the body of the article.

Conflicts of interest

The authors declare that they have no competing interests regarding the work presented in this paper.

Code availability

Not applicable to this study.

References

Adams K, Heidarzadeh M (2021) A multi-hazard risk model with cascading failure pathways for the

472 Dawlish (UK) railway using historical and contemporary data. International Journal of Disaster
473 Risk Reduction, 56: 102082. https://doi.org/10.1016/j.ijdrr.2021.102082.
474 Alcantara-Ayala I, Dominguez-Morales L (2008) The San Juan de Grijalva catastrophic
475 landslide, Chiapas, Mexico: lessons learnt. Edited by: Casagli N, Fanti R, Tofani V. Proc First
476 World Landslide Forum. 2008.
477 Aimaiti Y, Liu W, Yamazaki F, Maruyama Y (2019) Earthquake-induced landslide mapping for the
478 2018 Hokkaido Eastern Iburi Earthquake Using PALSAR-2 data. Remote Sensing 11(20):2351.
479 Ataie-Ashtiani B, Yavari-Ramshe S (2011) Numerical simulation of wave generated by landslide
480 incidents in dam reservoirs. Landslides 8(4):417-432.
481 Ataie-Ashtiani B, Nik-Khah A (2008). Impulsive waves caused by subaerial landslides. Environmental
482 Fluid Mechanics 8(3): 263-280.
483 Barla G, Paronuzzi P (2013) The 1963 Vajont landslide: 50th anniversary. Rock Mechanics and Rock
484 Engineering 46(6): 1267-1270
485 Bosa S, Petti M (2011) Shallow water numerical model of the wave generated by the Vajont
486 landslide. Environmental Modelling & Software 26(4):406-418.
487 Chang M, Zhou Y, Zhou C, Hales TC (2021) Coseismic landslides induced by the 2018 M w 6.6 Iburi,
488 Japan, Earthquake: spatial distribution, key factors weight, and susceptibility
489 regionalization. Landslides 18(2):755-772.
490 Chen G, Xia M, Thuy DT, Zhang Y (2021) A possible mechanism of earthquake-induced landslides

focusing on pulse-like ground motions. Landslides 18(5):1641-1657.

Dziewonski AM, Chou T-A, Woodhouse JH (1981) Determination of earthquake source parameters from waveform data for studies of global and regional seismicity. Journal of Geophysical Research 86(B4):2825–2852. https://doi.org/10.1029/JB086iB04p02825.

Ekström G, Nettles M, Dziewonski AM (2012) The global CMT project 2004–2010: Centroid-moment tensors for 13,017 earthquakes. Physics of the Earth and Planetary Interiors 200–201:1–9. https://doi.org/10.1016/j.pepi.2012.04.002

Ersoy H, Karahan M, Gelişli K, Akgün A, Anılan T, Sünnetci MO, Yahşi BK (2019) Modelling of the landslide-induced impulse waves in the Artvin Dam reservoir by empirical approach and 3D numerical simulation. Engineering Geology 249:112-128.

Evers FM, Boes RM (2019) Impulse Wave Runup on Steep to Vertical Slopes. Journal of Marine Science and Engineering 7 (1), 8. https://doi.org/10.3390/jmse7010008.

Evers F, Heller V, Fuchs H, Hager WH, Boes R (2019a) Landslide-generated Impulse Waves in Reservoirs: Basics and Computation. VAW-Mitteilungen 254.

Evers FM, Hager WH, Boes RM (2019b) Spatial Impulse Wave Generation and Propagation. Journal of Waterway, Port, Coastal, and Ocean Engineering 145, 04019011.

Franco A, Schneider-Muntau B, Roberts N J, Clague J J, Gems B (2021) Geometry-Based Preliminary Quantification of Landslide-Induced Impulse Wave Attenuation in Mountain Lakes. Applied Sciences 11(24): 11614. https://doi.org/10.3390/app112411614.

510 Fritz HM, Kalligeris N, Borrero JC, Broncano P, Ortega E (2008) The 15 August 2007 Peru tsunami
511 runup observations and modeling. Geophysical Research Letters 35(10).
512 Fritz HM, Hager WH, Minor HE (2004) Near field characteristics of landslide generated impulse
513 waves. Journal of Waterway Port Coastal and Ocean Engineering 130(6):287-302.
514 Gill JC, Malamud BD (2016) Hazard interactions and interaction networks (cascades) within
515 multi-hazard methodologies. Earth System Dynamics 7(3):659-679.
516 Heidarzadeh M, Teeuw R, Day S, Solana C (2018) Storm wave runups and sea level variations for the
517 September 2017 Hurricane Maria along the coast of Dominica, eastern Caribbean Sea: evidence
518 from field surveys and sea level data analysis. Coastal Engineering Journal 60(3):371–384.
519 https://doi.org/10.1080/21664250.2018.1546269
520 Heidarzadeh M, Putra PS, Nugroho HS, Rashid DBZ (2020) Field survey of tsunami heights and
521 runups following the 22 December 2018 Anak Krakatau volcano tsunami, Indonesia. Pure and
522 Applied Geophysics 177:4577–4595. https://doi.org/10.1007/s00024-020-02587-w.
523 Heidarzadeh M, Muhari A, Wijanarto AB (2019) Insights on the source of the 28 September 2018
524 Sulawesi tsunami, Indonesia based on spectral analyses and numerical simulations. Pure and
525 Applied Geophysics 176:25–43. https://doi.org/10.1007/s00024-018-2065-9.
526 Heidarzadeh M, Rabinovich A B (2021) Combined Hazard of Typhoon-Generated Meteorological
527 Tsunamis and Storm Surges along the Coast of Japan. Natural Hazards 106:1639–1672.
528 https://doi.org/10.1007/s11069-020-04448-0.

529 Heidarzadeh M, Satake K (2015) Source properties of the 17 July 1998 Papua New Guinea tsunami
530 based on tide gauge records. Geophysical Journal International, 202 (1): 361-369.
531 https://doi.org/10.1093/gji/ggv145.
532 Heller V, Hager WH (2010) Impulse Product Parameter in Landslide Generated Impulse Waves.
533 Journal of Waterway, Port, Coastal, and Ocean Engineering 136:145–155.
534 Heller V, Hager W H (2014) A universal parameter to predict subaerial landslide tsunamis?. Journal of
535 Marine Science and Engineering, 2(2): 400–412.
536 Heller V, Spinneken J (2015) On the effect of the water body geometry on landslide–tsunamis:
537 Physical insight from laboratory tests and 2D to 3D wave parameter transformation. Coastal
538 Engineering, 104: 113-134.
539 Heller V, Hager W H, Minor H E (2008) Scale effects in subaerial landslide generated impulse
540 waves. Experiments in Fluids, 44(5): 691-703.
541 Hermanns R L, Oppikofer T, Roberts N J, Sandøy G (2014) Catalogue of Historical Displacement
542 Waves and Landslide-Triggered Tsunamis in Norway. In: G. Lollino et al. (eds.), Engineering
543 Geology for Society and Territory – Volume 4, DOI: 10.1007/978-3-319-08660-6_13.
544 Huang B, Yin Y, Liu G, Wang S, Chen X, Huo Z (2012) Analysis of waves generated by Gongjiafang
545 landslide in Wu Gorge, three Gorges reservoir, on November 23, 2008. Landslides 9(3):395-405.
546 Japan Commission on Large Dams (2018) Dams in Japan: overview 2018. Online materials at:
547 https://jcold.or.jp/cm/wp-content/uploads/2020/01/Dams-in-Japan-2018-web%E7%94%A8.pdf

(page last accessed on 18th May 2021).

Kamphuis JW, Bowering RJ (1970) Impulse waves generated by landslides. In: Proceedings of the 12th Coastal Engineering Conference, ASCE, Reston Va. 1 575–588.

Katsumata K, Ichiyanagi M, Ohzono M, Aoyama H, Tanaka R, Takada M, Yamaguchi T, Okada K, Takahashi H, Sakai S, Matsumoto S, Okada T, Matsuzawa T, Hirano S, Terakawa T, Horikawa S, Kosuga M, Katao H, Iio Y, Nagaoka A, Tsumura N, Ueno T, the Group for the Aftershock Observations of the 2018 Hokkaido Eastern Iburi Earthquake, (2019) The 2018 Hokkaido Eastern Iburi earthquake (M_{JMA}= 6.7) was triggered by a strike-slip faulting in a stepover segment: insights from the aftershock distribution and the focal mechanism solution of the main shock. Earth Planets and Space 71:53. https://doi.org/10.1186/s40623-019-1032-8

Le TA, Takagi H, Heidarzadeh M, Takata Y, Takahashi A (2019) Field Surveys and Numerical Simulation of the 2018 Typhoon Jebi: Impact of High Waves and Storm Surge in Semi-enclosed Osaka Bay, Japan. Pure and Applied Geophysics 176(10):4139–4160. https://doi.org/10.1007/s00024-019-02295-0

Li R, Wang F, Zhang S (2020) Controlling role of Ta-d pumice on the coseismic landslides triggered by 2018 Hokkaido Eastern Iburi Earthquake. Landslides 17(5):1233-1250.

Liu B, Siu YL, Mitchell G (2016) Hazard interaction analysis for multi-hazard risk assessment: a systematic classification based on hazard-forming environment. Natural Hazards and Earth System Sciences 16(2):629-642.

567 Lu P, Shi W, Wang Q, Li Z, Qin Y, Fan X (2021) Co-seismic landslide mapping using Sentinel-2 10-m
568 fused NIR narrow, red-edge, and SWIR bands. Landslides 1-21.
569 Lyddon CE, Brown JM, Leonardi N, Saulter A, Plater AJ (2019) Quantification of the uncertainty in
570 coastal storm hazard predictions due to wave-current interaction and wind forcing. Geophysical
571 Research Letters 46(24):14576-14585.
572 Miyagi T, Yamashina S, Esaka F, Abe S (2011) Massive landslide triggered by 2008 Iwate–Miyagi
573 inland earthquake in the Aratozawa Dam area, Tohoku, Japan. Landslides 8(1):99-108.
574 Muhari A, Heidarzadeh M, Susmoro H, Nugroho HD, Kriswati E, Supartoyo Wijanarto AB, Imamura
575 F, Arikawa T (2019) The December 2018 Anak Krakatau volcano tsunami as inferred from
576 post-tsunami field surveys and spectral analysis. Pure and Applied Geophysics 176:5219–5233.
577 https://doi.org/10.1007/s00024-019-02358-2.
578 McCulloch D S (1966) Slide-induced waves, seiching, and ground fracturing caused by the earthquake
579 of March 27, 1964, at Kenai Lake, Alaska. Geological Survey Professional Paper 543-A.
580 McFall B C, Fritz H M (2016) Physical modelling of tsunamis generated by three-dimensional
581 deformable granular slides on planar and conical island slopes. Proceedings of Royal Society
582 London A 472 (2188): 20160052.
583 Mohammed F, Fritz H M (2012) Physical modeling of tsunamis generated by three-dimensional
584 deformable granular landslides. Journal of Geophysical Research Oceans 117 (C11),
585 https://doi.org/10.1029/2011JC007850.

586 Noda E (1970) Water waves generated by landslides. Journal of the Waterways, Harbors and Coastal
587 Engineering Division, 96(4): 835-855.
588 Omira R, Dogan GG, Hidayat R, Husrin S, Prasetya G, Annunziato A, Proietti C et al. (2019) The
589 September 28th, 2018, tsunami in Palu-Sulawesi, Indonesia: A post-event field survey. Pure and
590 Applied Geophysics 176 (4):1379-1395.
591 Oppikofer T, Hermanns R L, Roberts N J, Böhme M (2019) SPLASH: semi-empirical prediction of
592 landslide-generated displacement wave run-up heights. Geological Society, London, Special
593 Publications 477(1):353-366. https://doi.org/10.1144/SP477.1.
594 Osanai N, Yamada T, Hayashi SI, Kastura SY, Furuichi T, Yanai S, Murakami Y, Miyazaki T, Tanioka
595 Y, Takiguchi S, Miyazaki M (2019) Characteristics of landslides caused by the 2018 Hokkaido
596 Eastern Iburi Earthquake. Landslides 16(8):1517-1528.
597 Panizzo A, Girolamo PD, Risio MD, Maistri A, Petaccia A (2005) Great landslide events in Italian
598 artificial reservoirs. Natural Hazards and Earth System Sciences 5(5):733-740.
599 Roberts N J, McKillop R J, Lawrence M S, Psutka J F, Clague J J, Brideau M A, Ward B C (2013)
600 Impacts of the 2007 landslide-generated tsunami in Chehalis Lake, Canada. In: Landslide science
601 and practice (pp. 133-140). Springer, Berlin, Heidelberg. DOI: 10.1007/978-3-642-31319-6_19.
602 Robert N J, McKillop R, Hermanns R L, Clague J J, Oppikofer T (2014) Preliminary Global
603 Catalogue of Displacement Waves from Subaerial Landslides. In: Proc. Third World Landslide
604 Forum. K. Sassa et al. (eds.), Landslide Science for a Safer Geoenvironment, Vol. 3, DOI:

605 10.1007/978-3-319-04996-0_104.

606 Sabeti R, Heidarzadeh M (2020) Semi-empirical predictive equations for the initial amplitude of

607 submarine landslide-generated waves: applications to 1994 Skagway and 1998 Papua New

608 Guinea tsunamis. Natural Hazards 103:1591–1611. https://doi.org/10.1007/s11069-020-04050-4.

609 Savage B M, Johnson M C (2001) Flow over ogee spillway: Physical and numerical model case

610 study. Journal of hydraulic engineering 127(8): 640-649.

611 Slingerland R, Voight B (1982) Evaluating hazard of landslide-induced water waves. Journal of the

612 Waterway, Port, Coastal and Ocean Division 108(4): 504-512.

613 Schnitter G (1964) Die Katastrophe von Vaiont in Oberitalien, Wasser- und Energiewirtschaft 56(2/3)

614 61-69.

615 Schuster RL, Wieczorek GF (2002) Landslide triggers and types. In: Proceedings of the 1st European

616 Conference on Landslides, Editors: J. Rybář, J. Stemberk, P. Wagner, Prague, Czech Republic

617 59-78, Balkema, Tokyo.

618 Synolakis CE (1987) The runup of solitary waves. Journal of Fluid Mechanics 185:523-545.

619 Takagi H, Takahashi A (2021) Short-fetch high waves during the passage of 2019 Typhoon Faxai over

620 Tokyo Bay. Frontiers of Earth Science 15(2).

621 Takagi H, Pratama MB, Kurobe S, Esteban M, Aránguiz R, Ke B (2019) Analysis of generation and

622 arrival time of landslide tsunami to Palu City due to the 2018 Sulawesi earthquake.

623 Landslides 16(5):983-991.

624 Tsuji Y, Satake K, Ishibe T, Kusumoto S, Harada T, Nishiyama A, Kim H Y, Ueno T, Murotani S, Oki
625 S, Sugimoto M, Tomari J, Heidarzadeh M, Watada S, Imai K, Choi B H, Yoon S B, Bae J S, Kim
626 K O, and Kim H W (2011) Field surveys of tsunami heights from the 2011 Off the Pacific Coast
627 of Tohoku, Japan, earthquake. Bulletin of the Earthquake Research Institute University of Tokyo
628 86: 29–279 (in Japanese with English abstract).
629 Vacondio R, Mignosa P, Pagani S (2013) 3D SPH numerical simulation of the wave generated by the
630 Vajont rockslide. Advances in Water Resources 59(9):146-156.
631 Wang F, Fan X, Yunus AP, Subramanian SS, Alonso-Rodriguez A, Dai L, Xu Q, Huang R (2019)
632 Coseismic landslides triggered by the 2018 Hokkaido, Japan (M w 6.6), earthquake: spatial
633 distribution, controlling factors, and possible failure mechanism. Landslides 16(8):1551-1566.
634 Wessel P, Smith WHF (1998) New improved version of Generic Mapping Tools released. EOS
635 Transactions American Geophysical Union 79(47):579-579.
636 Xue H, Ma Q, Diao M, Jiang L (2019) Propagation characteristics of subaerial landslide-generated
637 impulse waves. Environmental Fluid Mechanics 19(1):203-230.
638 Yamagishi H, Yamazaki F (2018) Landslides by the 2018 Hokkaido Iburi-Tobu Earthquake on
639 September 6. Landslides 15 (12):2521-2524.
640 Yin YP, Huang B, Chen X, Liu G, Wang S (2015) Numerical analysis on wave generated by the
641 Qianjiangping landslide in Three Gorges Reservoir, China. Landslides 12(2):355-364.
642 Zhang S, Li R, Wang F, Iio A (2019) Characteristics of landslides triggered by the 2018 Hokkaido

643 Eastern Iburi earthquake, Northern Japan. Landslides 16(9):1691-1708.

644 Zhou JW, Xu FG, Yang XG, Yang YC, Lu PY (2016) Comprehensive analyses of the initiation and

645 landslide-generated wave processes of the 24 June 2015 Hongyanzi landslide at the Three Gorges

646 Reservoir, China. Landslides 13(3):589-601.

647

648

649

650 **Table captions:**

651

652 **Table 1.** Estimated dimensions and volumes of landslides. See Figures 1 and 6 for the locations of the
653 landslides. All of these six landslides entered the reservoir, but it is speculated that only three of
654 them (LS1, LS2 and LS3) were responsible for the observed runup.

655

656 **Table 2.** The maximum initial wave amplitude (a_M), the attenuated wave amplitude due to
657 propagation (a_m), and runup height (R_1 and R_2) estimated from various empirical equations for
658 the combination of three landsides of LS1, LS2, and LS3. The average value of drop heights for
659 LS1, LS2 and LS3 is used for calculations.

660

661

662 ***** End of Table captions *****

Figure captions:

Figure 1. a) Location of the Apporo dam and reservoir in Hokkaido, Japan and the epicenter of the earthquake. **b)** A satellite image from Google-Earth (https://earth.google.com/) showing the dam area after the earthquake and the location of six landslides (LS1 – LS6) near the dam body. **c), d), e)** Our field photos showing detailed views from the six landslides near the dam body. LS is an acronym for "landslide".

Figure 2. Apporo dam located in Hokkaido, Japan. **a)** A field photo showing the dam body and the reservoir. **b)** A cross-section of the dam showing that the dam is constructed from Cemented Sand and Gravel (CSG) with a 1.5 m concrete layer at the outer layer. This sketch is based on the dam body drawings provided to the first author by the site engineers during the surveys. **c)** A view of the dam crest and the downstream area. **d)** The entrance of the spillway. In panel "b", EL, NWL and masl are abbreviations for "Elevation", "Normal Water Level", and "meters above the sea level", respectively.

Figure 3. a) Rainfall records at Atsuma meteorological station operated by JMA spanning 2018. The times of the earthquake and Typhoon Jebi are marked in the figure by arrows. **b)** Surface air pressure at the time of Typhoon Jebi's approach to Hokkaido (17:00 UTC on 4 September 2018). **c)** Rain band induced by the Typhoon Jebi. The stars in panels "b" and "c" indicate the location of Atsuma Town. Surface air pressure and rainfall data are extracted using the typhoon model with the meso-scale weather forecasting model of the Japan Meteorological Agency (JMA-MSM) (Takagi and Takahashi 2021).

686

687 **Figure 4.** The mainshock and one-month aftershocks (M1 or larger) of the 5 September 2018
688 Hokkaido M_w 6.6 earthquake around the Apporo dam. **a)** Distribution of the one-month
689 aftershocks and the mainshock in the region relative to the dam site. **b)** Magnitude-time plot
690 indicated by the left vertical axis and the green bars and circles. The right vertical axis and the
691 thick blue curve indicate the cumulative number of aftershocks. The horizontal axis begins from
692 the earthquake origin time (i.e., 5 September 2018 UTC). Star shows the epicenter of the
693 earthquake.

694

695 **Figure 5.** Field survey photos of landslides following the September 2018 earthquake around the
696 Atsuma area of Hokkaido (Japan). **a)** A shallow landslide near a road. **b)** and **c)** A water treatment
697 plant destroyed by a landslide on a nearby slope. **d)** A shallow landslide near a road. **e)** A narrow
698 and shallow landslide. **f)** A large shallow landslide.

699

700 **Figure 6. a)** Characteristics and dimension estimates of landslides LS1, LS2 and LS3. The background
701 satellite image in panel "a" is from Google-Earth satellite images (https://earth.google.com/) but
702 the dimensions are based on our field surveys. **b), c), d), e), f)** Our field photos of the landslides
703 from our surveys.

704

705 **Figure 7.** Temporal variations of reservoir water level (blue) and reservoir storage volume (orange)
706 during the 2018 earthquake and consequent landslides. The vertical dashed line shows the origin
707 time of the earthquake. JST stands for Japan Standard Time. The term 'masl' represents 'meters
708 above the sea level'.

Figure 8. Measurement of the runup of the landslide-generated waves in the Apporo dam reservoir following the September 2018 Hokkaido earthquake. **a), b)** Runup measurement point showing the debris generated by landslide-generated wave. The inset at the upper-left of panel ”a” shows the runup measurement point. **c)** Sketch showing the definition of maximum initial wave amplitude (a_M), the attenuated wave amplitude due to propagation (a_m), and runup height (R).

Figure 9. Damage from the landslide-generated waves around the left bank of the Apporo dam reservoir following the September 2018 Hokkaido earthquake. This is the entrance of the opening that we measured runup (Figure 8). **a)** A photo from far showing the damaged reservoir bank revetment, the reservoir and the bridge passing through the reservoir. The box indicates the area enlarged in panel “b” of this figure. **b)** A close-up view of the damaged area, which is the area shown in a box in panel “a”.

***** End of Figure captions *****